Int. J. Electrochem. Sci., 11 **(2016)** 3876 - 3886

International Journal of
ELECTROCHEMICAL
SCIENCE
www.electrochemsci.org

Synthesis and Properties of Nitrogen-Doped Graphene as Anode Materials for Lithium-Ion Batteries

Changjing Fu[*], *Chunlai Song, Lilai Liu, Xuedong Xie, Weiling Zhao*

School of Materials Science and Engineering, Heilongjiang University of Science and Technology, 2468 Puyuan Road, Harbin 150022, P.R. China
[*]E-mail: fcj_hit@163.com

Received: 20 January 2016 / *Accepted:* 25 February 2016 / *Published:* 1 April 2016

Nitrogen-doped graphene (N-rGO) was successfully synthesized during the reduction of graphene oxide by the modified Hummers' method. In contrast to the reduced graphene oxide (rGO), N-rGO presented superior morphology, structure and composition as the anode of lithium-ion batteries (LIBs) according to the examination of SEM, TEM, XRD, Raman spectrum and XPS. The doping content of nitrogen in N-rGO was about 7.98 at.%. The electrochemical performances of N-rGO as anodes of LIBs were also evaluated accordingly. Thus-prepared N-rGO showed a higher reversible specific capacity of 332 mAh g^{-1} during 600 cycles at 500 mA·g^{-1}. Even at 4 A·g^{-1}, a reversible capacity of 208 mAh·g^{-1} can still be maintained. The improved electrochemical performance of N-rGO as anodes of LIBs could be due to the specific characteristics of the unique nanostructures, the covalent interactions between N and graphene, the good conductivity and high surface areas, which reduce the transfer resistance for Li-ion and electron and provide more extra live regions for Li storage.

Keywords: Lithium-ion batteries, Anode, N-rGO, Synthesis

1. INTRODUCTION

As a new class of two-dimensional carbon allotropes, graphene has attracted great attention in recent years due to its different structure from the precursor graphite [1,2]. It demonstrates many fascinating electronic and mechanical properties induced by its unique nanostructured sp^2 carbon materials, ultra-high surface area, high electrical conductivity and chemical stability [3,4]. It is therefore considered to be a promising candidate as the anode of lithium-ion batteries (LIBs) to replace

doi: 10.20964/110391

the commercialized graphite anode [5-7]. However, the low cycle life and the bad conductivity of the graphene anode impede its practical application.

Doping of heteroatoms into the carbon crystal lattice of graphene, such as nitrogen, silicon, sulfur and boron, could effectively tailor its electronic and chemical properties [8-10]. Among them, nitrogen-doped graphene is expected to enhance the performance of LIBs due to the more activated spaces, which facilitate the transport of Li atoms and electrons on graphene [11-14]. Recently, chemical method has been proved to be more effective in the synthesis of nitrogen doping graphene, because the nitrogen-doped graphene prepared by this method is with better conductivity [15-17]. Wang et al. [18] synthesized the high performance nitrogen-doped graphene (N-rGO) nanosheets through heat treatment of graphite oxide under an ammonia atmosphere and found that it delivered a high reversible capacity of 900 $mAh \cdot g^{-1}$ at 42 $mA \cdot g^{-1}$. Wu et al. [19] prepared N-rGO with the discharging capacity of 872 $mAh \cdot g^{-1}$ after 30 cycles at 50 $mA \cdot g^{-1}$, which is much higher than that of reduced graphene oxide (rGO) anode. However, reports on the preparation method of N-rGO are less and the heat treatment method under ammonia or nitrogen atmosphere is often used. Therefore, it is of paramount importance to develop a simple method for the synthesis of N-rGO.

In this work, liquid ammonia was cleverly selected as the nitrogen source, and the preparation of N-rGO and the reduction of graphene oxide were finished in one step. Furthermore, the thus-synthesized N-rGO exhibited excellent electrochemical performance. The composition and microstructure of N-rGO were also characterized and evaluated in detail.

2. EXPERIMENTAL

2.1 Preparation of N-rGO

Expanded graphite was oxidized in the modified Hummers method to obtain graphite oxide [20]. 1 g of expanded graphite with the expanded volume of 280, 0.5 g of sodium nitrate and 40 mL of sulfuric acid (98 wt.%) were mixed together in an ice-water bath below 1^{o}C. Potassium permanganate, the oxidant, was added slowly into the solution at a speed of 0.5 g·5 min^{-1} and the total amount of the oxidant was controlled at 5 g. Then, thus-prepared mixture was heated at 35^{o}C for 30 min. After that, 40 mL of hot water was added into the mixture and the temperature of the mixture increased quickly to 98 ^{o}C in this step and remained 1 h in the hot-water bath of the same temperature. Subsequently, a certain amount of H_2O_2 (60 wt.%) was used to dissolve the excess MnO_2. The suspension was finally washed with dilute hydrochloric acid and deionized water for several times until the pH value of the leached solution was neutral. Thus, graphene oxide was synthesized, which was further reduced by the solvothermal method. 30 mL of the as-prepared graphene oxide was poured into an steel autoclave, which was subsequently added with 1 mL of ammonia (37 vol.%) before heat-treated at 180^{o}C for 2 h. The black suspended particles were collected and washed with stilled water and ethanol, and then placed in a freeze-dryer for 2 days. The rGO was also synthesized in the same way, just without the addition of ammonium hydroxide during the process of graphene oxide reduction, for reference.

2.2 Materials characterization

Powder X-ray diffraction analyses were carried out on D/max 2550-PC diffractometer with Cu *K*a radiation (λ=0.15406 nm) and the scanning angle (2θ) ranged from 10^o to 90^o. The scanning rate was controlled at $5^o \cdot min^{-1}$. Scanning electron microscopy (SEM) images were performed with an S-4700 microscope and transmission electron microscopy (TEM) images were taken with a JEOL-2100F microscope. The electronic and chemical states of samples were examined by X-ray photoelectron spectroscopy (XPS, Kratos Analytical). Raman spectra were recorded on a WITec CRM200 confocal Raman microscopy. The wavelength and the spot size of the laser were 514.5 nm and 2 μm, respectively.

2.3 Electrochemical Measurements

CR2025 type coin cells were used to perform the electrochemical tests. The electrode powder was composed of N-rGO (rGO) (80 wt.%), carbon black (10 wt.%), and polyvinylidene fluoride (PVDF) binder(10 wt.%). After mixing, the mixture was dissolved in N-methyl pyrrolidinone (NMP) to prepare slurry, which was then spread onto copper foil using a doctor-blade. The as-prepared electrode film was following transferred into a vacuum drying oven to dry. Taking lithium-metal foils as the counter electrode and the reference electrode, and the polypropylene as the separator, cells were assembled in an argon-filled glovebox. The electrolyte was 1 $mol \cdot L^{-1}$ $LiPF_6$ dissolved in the mixed solution of ethylene carbonate (EC) and dimethyl carbonate (DMC) in the same weight percentage. Before electrochemical measurements, the assembled cells were laid aside overnight to ensure that the separator and electrode were completely soaked by the electrolyte. Cyclic voltammetry measurements of the electrode were taken on a CHI660C electrochemical workstation with a scan rate of 0.1 $mV \cdot s^{-1}$. Galvanostatic charge and discharge measurements were conducted on a NEWARE battery tester with the cut-off voltage of 0.01 and 3.0 V (*vs*. Li^+/Li). Electrochemical impedance spectra (EIS) were recorded using a Princeton electrochemical workstation (M2273) from 10 mHz to 100 kHz with an alternate current amplitude of 5 mV. The electrochemical test temperature was 25±1 ^oC.

3. RESULTS AND DISCUSSION

3.1 Characterization of morphology and structure

The SEM and TEM images of the prepared N-rGO are presents in fig.1. Figure 1a shows that N-rGO still maintains the 2D ultrathin flexible structure of the pristine graphene, but has more corrugations and scrolling than the pristine graphene. They formed fluffy agglomerates, made even more extra pores and thus created higher surface areas. Figure 1b reveals that the fluffy structure of N-rGO could still be remained perfectly without any detected collapse even after drying, which may be associated with the intrinsic structure characters of graphene. The TEM observation of the N-rGO at

different position is shown in fig.1c and fig.1d. Large N-rGO nanosheets look like the thin silk with different thickness or layers. They are crumple, rise and fall like waves.

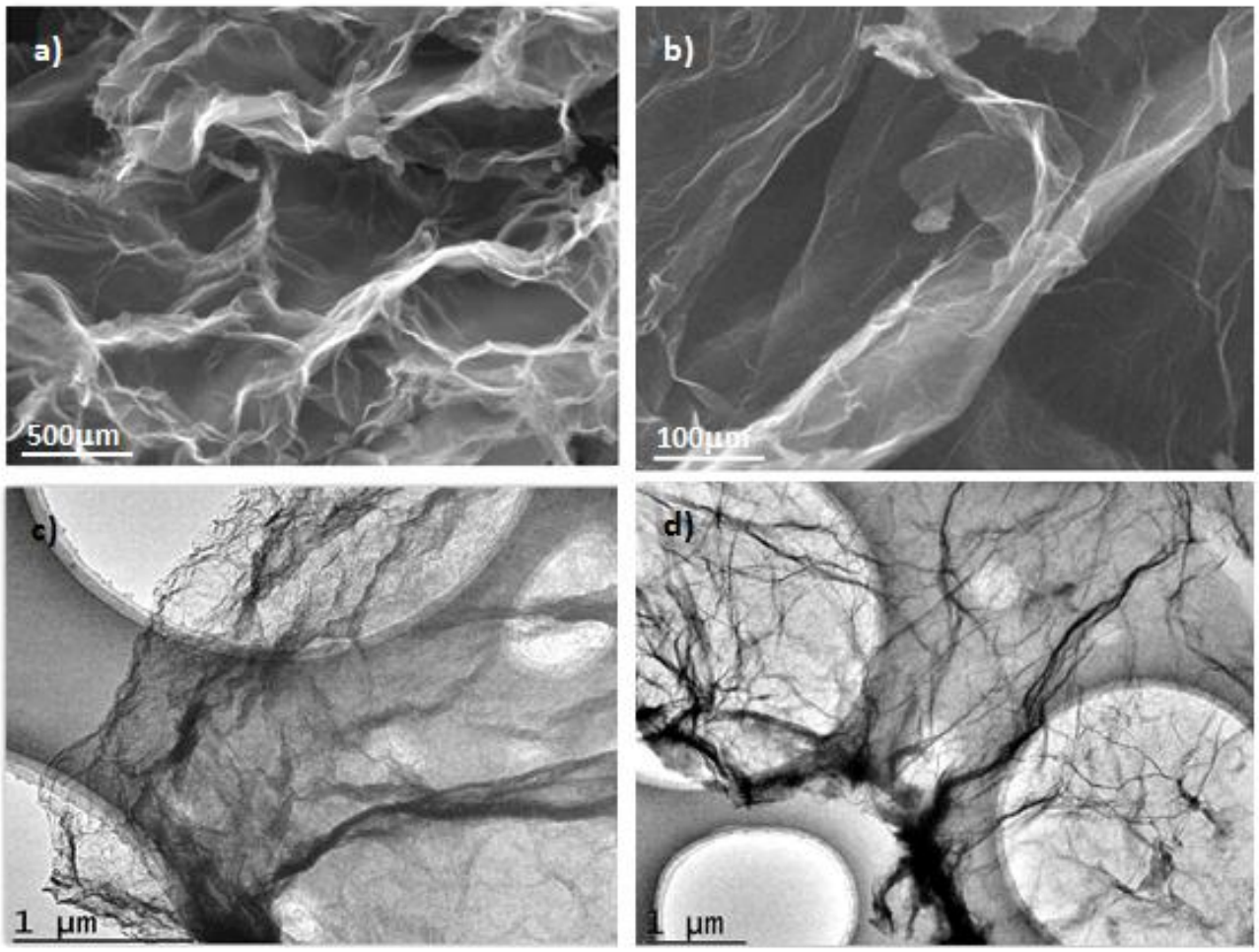

Figure 1. SEM images of N-rGO(a, b) and TEM images of N-rGO(c,d).

The thicker N-rGO sheets looks like clouds and intertangled together, as shown in fig.1c. While the thinner ones seem like the crumpled silk, they are transparent and with a large amount of wrinkles (fig.1d) indicating that they are composed of few layered graphene sheets. As reported previously, this kind of crumpling microstructure confirms the thermodynamic stability of the plannar graphene. Indeed, the representative TEM images of graphene prepared by the modified hummer's method from natural graphite have been proved to be with the similar few-layer and multilayer structure to that shown in fig.1c and fig.1d. The thin winkled structure of N-rGO is the same as the morphology that the graphene owns intrinsically [21], revealing that nitrogen doping doesn't change the microstructure of graphene. Moreover, it is this unique structure that ensures the N-rGO with more active regions to storage lithium ions.

3.2 Phase and composition analysis

Figure 2a shows the differences of phase composition between rGO and N-rGO. Although the doping of nitrogen in N-rGO is in a small amount, differences between rGO and N-rGO can be clarified easily. The XRD pattern of rGO exhibits a characteristic (002) peak of graphite emerged at 24.2°. Compared with rGO, it is found that the (002) peak of N-rGO appears at 26.3°, which indicates that nitrogen atoms has entered into the crystal lattice of graphite and caused the increased distance between the graphite layers. Moreover, XRD results further reveal that using this preparation method, the graphene oxides are almost completely reduced [22-24].

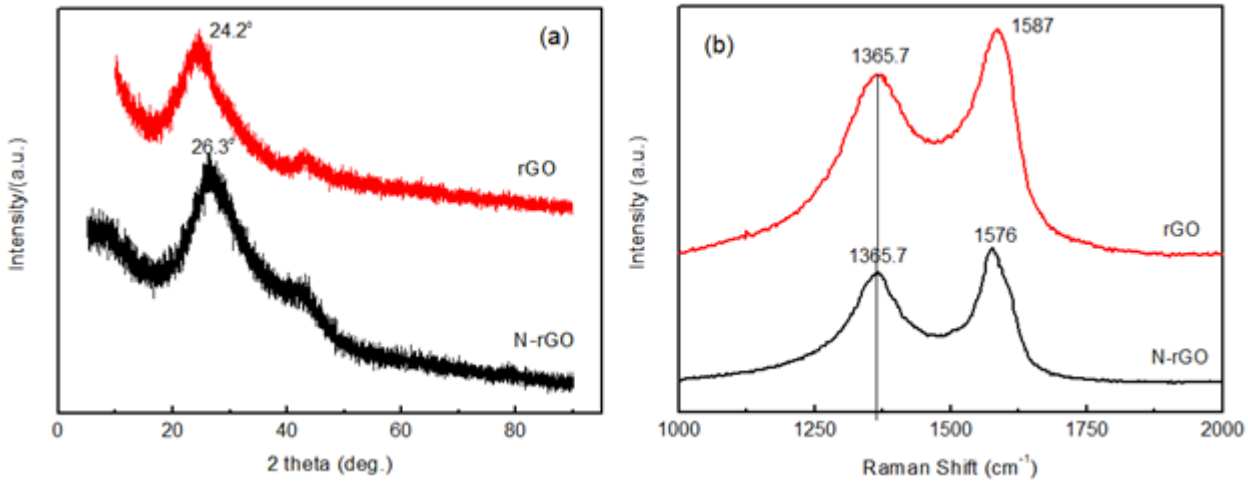

Figure 2. XRD patterns of N-rGO (a) and Raman spectra of N-rGO (b).

Figure 2b displays the Raman spectra of rGO and N-rGO, both of which present two obvious peaks of the D band and G band. They are the representative characteristics of graphene prepared by the chemical method [25-27]. The intensity of D band and G band are respectively corresponding to the disorder degree and the first-order scattering of the stretching vibration mode (E_{2g}) of sp^2 carbon. The D band and G band of rGO appear at 1365.7 cm^{-1} and 1587 cm^{-1}, respectively. However, the G band of N-rGO is down-shifted to 1576 cm^{-1} compared with the rGO sheets (1587 cm^{-1}). The down shift of the G band of N-rGO may be due to the strong capability of nitrogen heteroatoms in electron donating and the structural distortion of graphene induced by the different bond length between C-C and C-N [28]. Additionally, the integral intensity ratio of D band and G band (I_D/I_G) is usually used to measure the disorder of carbon-containing materials [29]. The I_D/I_G of N-rGO is obviously higher than that of rGO (1.29 for N-rGO and 1.15 for rGO), suggesting that N-rGO are even more disordered than rGO, which is in agreement with the microstructure observation of TEM and SEM. Besides that, there are more cavities and/or holes and/or defects in N-rGO that are convenient for lithium-storage [30]. On the other hand, the larger I_D/I_G and down-shift of the G band of N-rGO, as shown in fig.2b, further confirm the nitrogen doping in graphene.

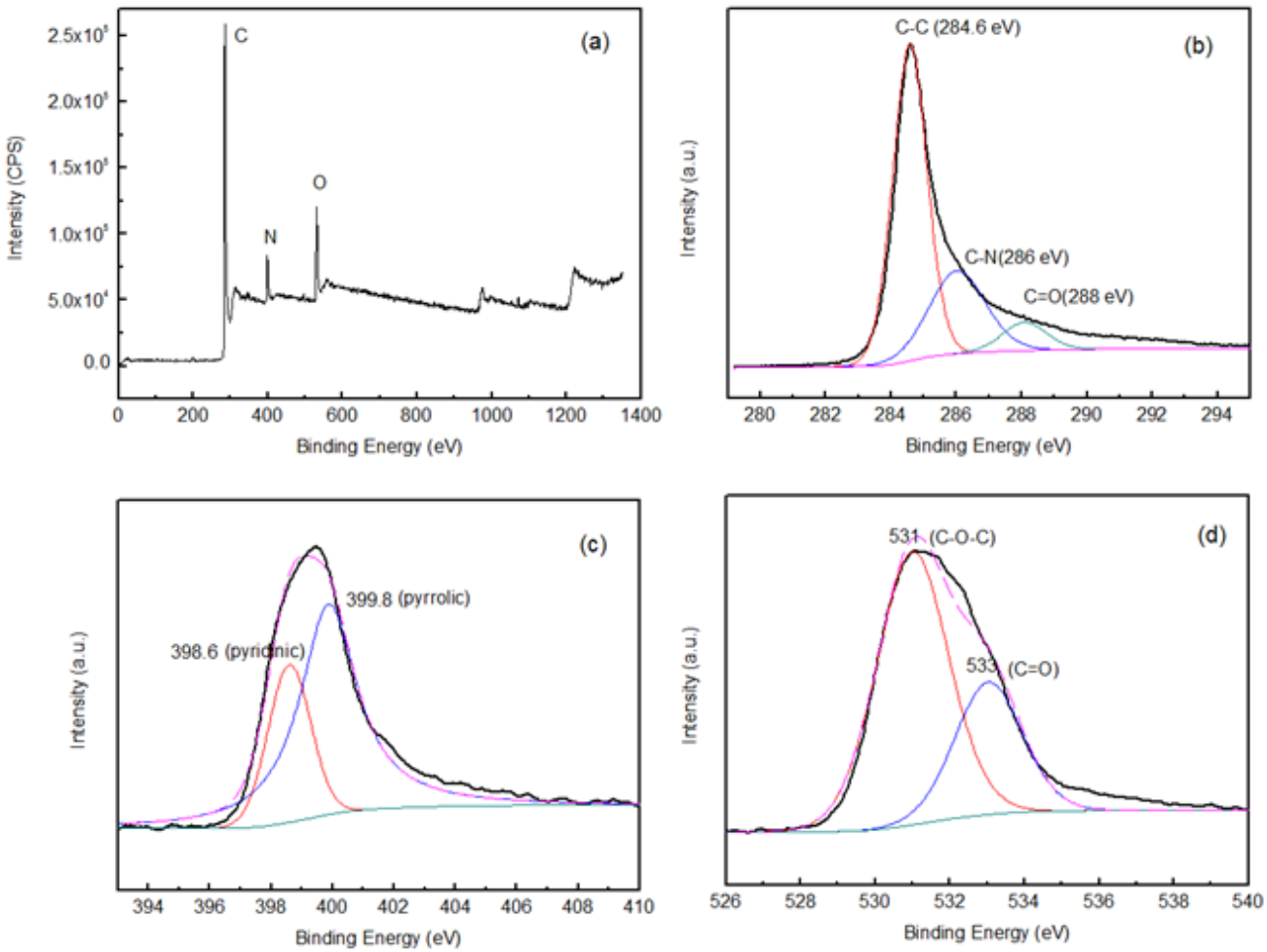

Figure 3. XPS spectra of N-rGO (a), and its C_{1s} spectra (b), N_{1s} spectra (c) and O_{1s} spectra (d).

In order to examine the elemental composition, chemical state and electronic state of the N-rGO, XPS was used to analyze its surface chemistry. The survey scan spectrum (fig.3a) showed the presence of the principle C_{1s}, O_{1s} and N_{1s} core levels with no evidence of impurities. Also it revealed that N content of N-rGO is c.a. 7.98 at.%. The C_{1s} spectra of N-rGO are presented in fig. 3b. According to C_{1s} fitting result of N-rGO in fig.3b, the peaks of carbon-containing groups appear at 284.6 eV (C-C), 286.0 eV (C-N) and 288 eV (C=O), respectively. The nitrogen-containing groups in the N-rGO are pyridinic N at ca. 398.6 eV and pyrrolic N at ca. 399.8 eV, respectively, as shown in fig.3c. As the carbon atoms on the edges or defect sites are even more active in chemistry than those within the plane of graphene, they are easily substituted by nitrogen and form the pyridinic N and pyrrolic N [31]. Additionally, the high-resolution O_{1s} XPS spectra (fig.3d) of N-rGO provide more in-depth information on the electronic state of N-rGO. The O_{1s} peaks of N-rGO matched well with two peaks at 531 eV and 533 eV, respectively. The peak at 531 eV was associated with the C-O-C group, while the one at 533 eV was corresponding to O=C in graphene nanosheets. In particular, the oxygen content of N-rGO was only 10.95%, which was 20.23% lower than that of GO, [20], suggesting that more of the oxygen-containing functional groups were removed with the help of nitrogen doping. The

reactions between the oxygen-containing groups of graphene oxide and ammonia facilitate the doping of nitrogen and the formation of C-N bonds [32].

3.3 Electrochemical performance

Figure 4a presents the cyclic voltammetry (CV) behavior of N-rGO. The CV curves of N-rGO and rGO are similar [33], suggesting that nitrogen doping has no visible impact on the initial lithium storage.

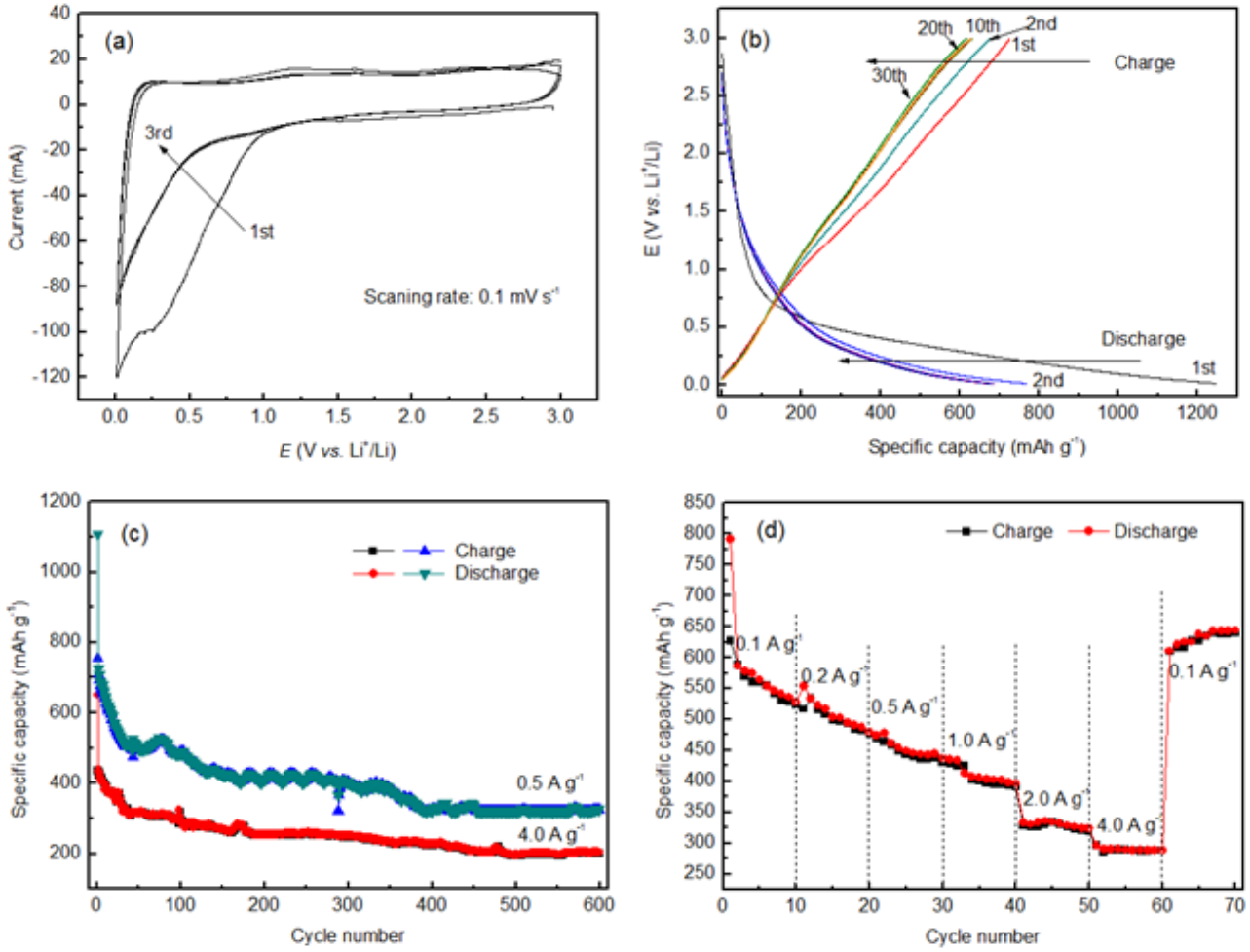

Figure 4. Cyclic voltammograms (CV) of N-rGO in the voltage range of 0-3.0 V at a scanning rate of 0.1 mV s^{-1} (a), discharge/charge curves of N-rGO at 100 mA g^{-1} (b), cycling performance of N-rGO at 0.5 and 4.0 A g^{-1}, respectively (c) and (d) rate performance for N-rGO electrode.

The reduction potential associated with lithium insertion approaches 0 V versus the Li^+/Li reference electrode, whereas the oxygen potential corresponding to lithium deintercalation is between 0.2 V and 0.3 V. In the first cycle, the formation of the solid electrolyte interface (SEI) on the anode induces to an obvious peak appeared at c.a. 0.24 V during the reduction of N-rGO, which disappears

since the second discharge. This reveals that a dense SEI film has formed on the surface of the anodes during the first discharge which effectively isolates the anode and the electrolyte during the following discharge cycles. Meanwhile, the anodic peak presents at 0.21 V. Compared with the first cycle, there is no obvious changes appeared on the charge/discharge curves since the second cycle, suggesting that lithium could reversibly intercalate and deintercalate into N-rGO layers.

The electrochemical properties of N-rGO as the anode of LIBs were conducted in a two-electrode cell. Figure 4b presents the charge/discharge curves of the 1st, 2nd, 10th, 20th and 30th cycle of N-rGO electrode in the voltage range of 0.01 to 3.0 V (*vs.* Li^+/Li) at 100 $mA \cdot g^{-1}$. The charge and discharge behavior of N-rGO is similar to that of graphene nanosheets. Both of them are with a large discharge/charge voltage hysteresis, high irreversible capacity and without distinguishable discharge plateaus [19]. The charge and discharge capacity of N-rGO electrode were 732.5 mAh $\cdot g^{-1}$ and 1245 mAh $\cdot g^{-1}$, respectively, at the first cycle with a coulombic efficiency of 59%. It is the decomposition of electrolyte at the electrode surface and the formation of solid electrolyte interphase (SEI) layer inducing to the large irreversible capacity of N-rGO electrode in the first cycle [34]. Since the second cycle, the discharge/charge profiles tended to stability indicating the formation of complete SEI film during the first cycle, which is consistent with the CV examination. The columbic efficiency was more than 91% from the 10^{th} cycle.

Figure 4c shows the cycle stability of N-rGO electrode at 0.5 and 4 $A \cdot g^{-1}$, respectively. It presents the similar cycle properties to the other LIBs' anodes. In the first 50 cycles, the specific capacity of N-rGO electrode declined gradually with the increase of cycling time and then tends to be stable. The reversible discharge specific capacity maintained at 332 $mAh \cdot g^{-1}$ at 0.5 $A \cdot g^{-1}$ after 600 cycles, demonstrating 45.5% retention of the second cycle capacity. Whereas at 4 $A \cdot g^{-1}$, the reversible discharge specific capacity maintained at 208 $mAh \cdot g^{-1}$ after 600 cycles, revealing that even at a higher current density, N-rGO prepared by the hydrothermal method still presented stable cycling performance. The reason might be due to the N-doping making the formation of carbon vacancies within a predominantly hexagonal graphene network [35], which results in the increase of the Li^+ storage sites of N-rGO [36]. Moreover, according to the XPS observation, N-rGO has a higher percentage of pyridinic N atoms that could greatly enhance the reversible capacity of N-containing electrodes because of the stronger electronegativity of nitrogen compared to carbon [37].

The rate performance of N-rGO electrode at different current densities of 0.1 $A \cdot g^{-1}$, 0.2 $A \cdot g^{-1}$, 0.5$A \cdot g^{-1}$, 1 $A \cdot g^{-1}$, 2 $A \cdot g^{-1}$ and 4 $A \cdot g^{-1}$ are presented in fig.4d. The reversible capacity tended to be remained at 530 $mAh \cdot g^{-1}$ after 10 cycles at 0.1 $A \cdot g^{-1}$. With the increase of the current density to 0.2, 0.5, 1.0, 2.0 and 4.0 $A \cdot g^{-1}$, respectively, the reversible discharge capacity sustained at 485, 446, 396, 324 and 290 $mAh \cdot g^{-1}$, respectively, much higher than that of the rGO electrode, especially at higher current densities. The reversible discharge capacities of rGO were 415, 342, 307 and 166 $mAh \cdot g^{-1}$ at the current densities of 0.2, 0.4, 0.8 and 4 $A \cdot g^{-1}$, respectively [18]. Furthermore, due to the gradual activation of electrode during the cycling process, the charge/discharge capacities of N-rGO anode were sustained or even with a slight increase when the current density returned to the initial 0.1 $A \cdot g^{-1}$ after 60 cycles. The reversible discharge capacity was 645 $mAh \cdot g^{-1}$ at 0.1 $A \cdot g^{-1}$, which was 21.7% higher than that of N-rGO anode in the first 10 cycles at the same current density. The excellent rate capability of N-rGO anode proves that it is a promising anode for high power LIBs. The covalent

interaction between nitrogen and graphene (C-N) induces to the fast electron transfer and so as to results in a higher rate performance of the anode.

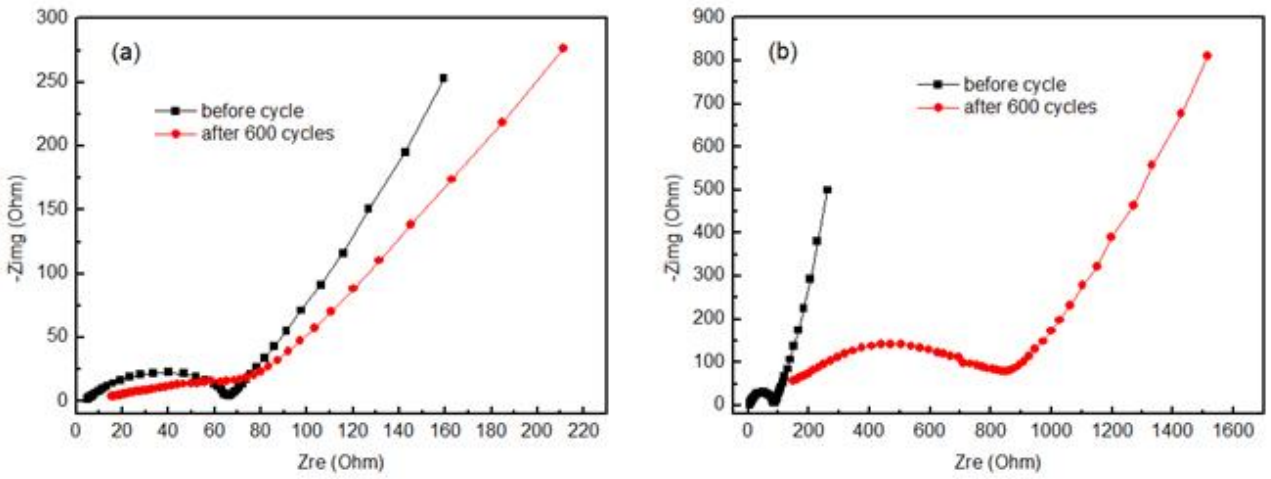

Figure 5. (a) Nyquist plots of N-rGO under 0.5 A g^{-1} and (b) Nyquist plots of N-rGO under 4 A g^{-1}.

In order to make clear the reasons resulted in the reduced reversible discharge capacity with the increase of cycling times, EIS analysis were further conducted, as shown in fig.5. In lithium-ion batteries, the rate capability of the electrode is determined by the charge transfer rate, and represented by the charge transfer resistance in the Nyquist plot of EIS. In the Nyquist plot, the semicircle appeared in the medium frequency range is usually corresponding to the charge-transfer resistance (R_{ct}) happening at the interface of electrode and electrolyte. While the straight line represents the so-called Warburg diffusion, is associated with the diffusion of lithium ions into electrodes. For the N-rGO anode cycled at 0.5 $A \cdot g^{-1}$ (fig.5a), R_{ct} was 61 Ω before cycles and decreased to 55 Ω after 600 cycles (ΔR_{ct}=-6 Ω). The reduced R_{ct} indicates that the charge transfer process was improved with cycles, revealing that the N-rGO anode was with a relatively stable conductivity network and microstructure. While the ohmic resistance of the sample increased more than 2 times inducing to the degradation of the electrode performance during cycling. ΔR_{ct} of the N-rGO anode cycled at 4 $A \cdot g^{-1}$ (fig.5b) was 619.5 Ω after 600 cycles, more than 7 times that of the sample without cycle. However, the R_{Ω} of the sample was 38.5 times that of the sample without cycle. Although the great increase of R_{Ω} is the main reason caused to the reduced capacity of N-rGO electrode at high current densities, the slow interfacial reaction kinetics retarded primarily the electrochemical Li storage performance of the electrode. Therefore, according to the EIS analysis, it is easy to make a conclusion that the reduced cycling capability of N-rGO anode was due to the great increase of ohmic resistance (R_{Ω}) with cycles, especially at high current densities, while the increase of the resistances for the charge transfer and Li^+ diffusion was relatively slightly. The postmortem examine presented that part of the N-rGO anode had peeled off from the surface of the Cu foil after 600 cycles, which may be one of the main reasons resulting in the increase of R_{Ω}.

4. CONCLUSIONS

In this article, N-rGO was synthesized by a novel method and it demonstrated excellent lithium storage properties as the anode of LIBs. The interface wettability between the electrode and electrolyte and the capability for lithium storage were extremely improved. Moreover, nitrogen atoms in the plane of graphene facilitate the transfer of lithium ions and electrons. The nitrogen-doping on the carbon crystal lattice of graphene induces the increase of the defect sites and vacancies as Li^+ active sites on the surface of graphene nanosheets, resulting in the increase of charge/discharge capacity and even higher reversible capacity. This study will pave a new way for the design and synthesis of the anode for LIBs. However, the bad adhesion between N-rGO electrode and copper foil during cycles is the main problem urgently to be solved.

ACKNOWLEDGEMENT
This work was supported by Heilongjiang Provincial Natural Science Foundation (B201416) and Scientific Research Starting Foundation for the Returned Oversea Chinese Scholars, Heilongjiang Province.

References

1. S. Park and R.S. Ruoff, *Nat. Nanotechnol*., 4 (2009) 217.
2. K.S. Novoselov, A.K. Geim and S.V. Morozov, *Science*, 306 (2004) 666.
3. M. Orlita, C. Faugeras and P. Plochocka, *Phys. Rev. Lett*., 101 (2008) 267601.
4. A.K. Geim and K.S. Novoselov, *Nat. Mater*., 6 (2007) 183.
5. A.N. Kotov, *Nature*, 442 (2006) 254.
6. D.D. Cai, L.X. Ding, S. Wang, Z. Li, M. Zhu and H.H. Wang, *Electrochim. Acta*, 139 (2014) 96.
7. S. Petnikota, S.K. Marka, A. Banerjee, M.V. Reddy, V.V.S.S. Srikanth, B.V.R. Chowdari, *J. Power Sources*, 293 (2015) 253.
8. X. Wang, X. Li and L. Zhang, *Science*, 324 (2009) 768.
9. D. Wei, Y. Liu and Y. Wang, *Nano Lett*., 9 (2009) 1752.
10. L.S. Panchakarla, K.S. Subrahmanyam and S.K. Saha, *Adv. Mater*., 4 (2009) 4726.
11. M. Morita, T. Hanada and H. Tsutsumi, *J. Electrochem. Soc*., 139 (1992) 1227.
12. X.L. Yu, C.Z. Zhan, R.T. Lv, Y. Bai, Y.X. Lin, Z.H. Huang, W.C. Shen, X.P. Qiu, F.Y. Kang, *Nano Energy*, 15 (2015) 43.
13. X.X. Liu, D.L. Chao, Y. Li, J. Hao, X.S. Liu, J.P. Zhao, J.Y. Lin, H.J. Fan, Z.X. Shen, *Nano Energy*, 17 (2015) 43.
14. Y.J. Cho, H.S. Kim and H. Im, *J. Phys. Chem. C*, 115 (2011) 9451.
15. D. Yu, L. Wei and W. Jiang, *Nanoscale*, 5 (2013) 3457.
16. Q.H. Liu, Z.J. Wu, Z.L. Ma, S. Dou, J.H. Wu, L. Tao, X. Wang, A.L. Shen and S.Y. Wang, *Electrochim. Acta*, 177 (2015) 298.
17. M. Du, J. Sun, J. Chang, F. Yang, L.J. Shi and L. Gao, *RCS adv*., 4 (2014) 42414.
18. H. Wang, C. Zhang and Z. Liu, *Mater. Chem*., 21 (2011) 5430.
19. Z.S. Wu, W.C. Ren, L. Wu, T. Li and H.M. Cheng, *ACS Nano*, 5 (2011) 5463.
20. C.J. Fu, G.G. Zhao, H.J. Zhang and S. Li, *Inter. J. Electrochem. Sci*., 8 (2013) 6269.
21. Z.L. Wang, D. Wu, Y. Huang, Z. Wu, L. Wang and X. Zhang, *Chem. Commun*., 48 (2012) 976.
22. J.C. Meyer, A.K. Geim, M.I. Katsnelson, K.S. Novoselov, T.J. Booth and S. Roth, *Nature*, 446 (2007) 60.
23. W. Gao, L.B. Alemany, L. Ci and P.M. Ajayan, *Nat. Chem*., 1 (2009) 403.

24. Z.J. Fan, W. Kai, J. Yan, T. Wei, L.J. Zhi, J. Feng, Y.M. Ren, L.P. Song and F. Wei, *ACS Nano*, 5 (2011) 191.
25. K.N. Kudin, B. Ozbas, H.C. Schniepp, R.K. Prudhomme, I.A. Aksay and R. Car, *Nano Lett.*, 8 (2008) 36.
26. Z.S. Wu, W.C. Ren, L.B. Gao, J.P. Zhao, Z.P. Chen, B.L. Liu, P.M. Tang, B. Yu, C.B. Jiang and H.M. Cheng, *ACS Nano*, 3 (2009) 411.
27. N. Soin, S.S. Roy, S. Roy, K.S. Hazra, D.S. Misra, T.H. Liu, C.J. Hetherlington and J.A. McLaughlin, *J. Phys. Chem. C*, 115 (2011) 5366.
28. Z. Lin, G. Waller, Y. Liu and C.P. Wang, *Adv. Energy Mater*., 2 (2012) 884.
29. B.D. Guo, Q.A. Liu, E.D. Chen, H.W. Zhu, L.A. Fang and J.R. Gong, *Nano Lett*., 10 (2010) 4975.
30. Y.C. Lin and P.W. Chiu, *Appl. Phys. Lett*., 96 (2010) 133110.
31. D.H. Deng, X.L. Pan, L.A. Yu, Y. Cui, Y.P. Jiang, J. Qi, W.X. Li, Q.A. Fu, X.C. Ma and Q.K. Xue, *Chem. Mater*., 23 (2011) 1188.
32. P. Lian, X. Zhu, S. Liang, Z. Li, W. Yang and H. Wang, *Electrochim. Acta*, 55 (2010) 3909.
33. X. Li, D. Geng, Y. Zhang, X. Meng, R. Li and X. Sun, *Electrochem. Commun*., 13 (2011) 822.
34. E. Strauss, G. Ardel, V. Livshits, L. Burstein, D. Golodnitsky and E. Peled, *J. Power Sources*, 88 (2000) 206.
35. N.A. Kaskhedikar and J. Maier, *Adv. Mater*., 21 (2009) 2664.
36. Y.P. Wu, S.B. Fang, W.G. Ju and Y.Y. Jiang, *J. Power Sources*, 70 (1998) 114.
37. E. Yoo, J. Nakamura and H. Zhou, *Energy Environ. Sci*., 5 (2012) 6928.